Chemistry–A European Journal

Research Article
doi.org/10.1002/chem.202303146

Chemistry Europe
European Chemical Societies Publishing

www.chemeurj.org

Influence of Crystallographic Structure and Metal Vacancies on the Oxygen Evolution Reaction Performance of Ni-based Layered Hydroxides**

Roger Sanchis-Gual[+],[a] Camilo Jaramillo-Hernández[+],[a] Diego Hunt[+],[b] Álvaro Seijas-Da Silva,[a] Martín Mizrahi,[c, d] Carlo Marini,[e] Víctor Oestreicher,*[a] and Gonzalo Abellán*[a]

Nickel-based layered hydroxides (LHs) are a family of efficient electrocatalysts for the alkaline oxygen evolution reaction (OER). Nevertheless, fundamental aspects such as the influence of the crystalline structure and the role of lattice distortion of the catalytic sites remain poorly understood and typically muddled. Herein, we carried out a comprehensive investigation on α-LH, β-LH and layered double hydroxide (LDH) phases by means of structural, spectroscopical, *in-silico* and electrochemical studies, which suggest the key aspect exerted by Ni-vacancies in the α-LH structure. Density functional theory (DFT) calculations and X-ray absorption spectroscopy (XAS) confirm that the presence of Ni-vacancies produces acute distortions of the electroactive Ni sites (reflected as the shortening of the Ni–O distances and changes in the O–Ni–O angles), triggering the appearance of Ni localised electronic states on the Fermi level, reducing the Egap, and consequently, increasing the reactivity of the electroactive sites in the α-LH structure. Furthermore, *post-mortem* Raman and XAS measurements unveil its transformation into a highly reactive oxyhydroxide-like phase that remains stable under ambient conditions. Hence, this work pinpoints the critical role of the crystalline structure as well as the electronic properties of LH structures on their inherent electrochemical reactivity towards OER catalysis. We envision Ni-based α-LH as a perfect platform for hosting trivalent cations, closing the gap toward the next generation of benchmark efficient earth-abundant electrocatalysts.

Introduction

Water electrolysis is considered one of the cleanest ways for producing hydrogen.[1–3] Nevertheless, its production also involves the oxygen evolution reaction (OER), an electrochemical process that requires high voltages because of slow kinetics. This process represents an important energetic efficiency loss in water-splitting systems and necessitates the use of inexpensive catalysts to reduce the energy barriers.[4,5] In this regard, the last decade has witnessed efforts in the development of earth-abundant electrocatalysts to reduce energy costs, with nickel-based materials emerging as one of the most widely used among the reported non-precious metal OER catalysts.[6]

Layered hydroxides (LHs) have been demonstrated to be outstanding OER electrocatalysts.[7–14] In addition to their exciting electrochemical features, they are easily scalable, affordable and composed of non-geolocalised abundant elements.[15–18] Furthermore, their high chemical versatility has allowed for the fabrication of compounds with improved parameters, thereby boosting the OER. Along this front, the effect of different morphologies,[19] interlayer spaces,[20] metallic compositions,[21] clustering and structural instabilities,[22] to name a few, have already been investigated. Catalytic improve-

[a] Dr. R. Sanchis-Gual,[+] C. Jaramillo-Hernández,[+] Á. Seijas-Da Silva, Dr. V. Oestreicher, Dr. G. Abellán
Instituto de Ciencia Molecular (ICMol)
Universidad de Valencia
Catedrático José Beltrán 2, 46980, Paterna, Valencia (Spain)
E-mail: victor.oestreicher@uv.es
gonzalo.abellan@uv.es
Homepage: www.icmol.es/2dchem

[b] Dr. D. Hunt[+]
Departamento de Física de la Materia Condensada, GiyA
Instituto de Nanociencia y Nanotecnología, CNEA-CAC-CONICET
Av. Gral. Paz, 1650, San Martín, Buenos Aires (Argentina)

[c] Dr. M. Mizrahi
Instituto de Investigaciones Fisicoquímicas Técnicas y Aplicadas (INIFTA)
Departamento de Química, Facultad de Ciencias Exactas
Universidad Nacional de La Plata
CCT La Plata- CONICET. Diagonal 113 y 64, 1900, La Plata (Argentina)

[d] Dr. M. Mizrahi
Facultad de Ingeniería
Universidad Nacional de La Plata
Calle 1 esq. 47, 1900, La Plata (Argentina)

[e] Dr. C. Marini
CELLS-ALBA Synchrotron
Cerdanyola del Vallès, 08290, Barcelona (Spain)

[+] These Authors contributed equally to this work.

[**] A previous version of this manuscript has been deposited on a preprint server (https://doi.org/10.26434/chemrxiv-2023-r5zqx)

Supporting information for this article is available on the WWW under https://doi.org/10.1002/chem.202303146

ments are typically the result of increased surface areas, the ability to adsorb OH ions, diffusion properties, and/or the intrinsic activities of electroactive sites. Nowadays, many parameters influencing the OER are still not completely well understood or even explored. In particular, fundamental aspects such as the specific role of the crystalline LH structure, as well as the coordination environment and cation distortions, have not been comprehensively studied for nickel centres.[23]

This is quite striking given the variety of crystalline structures that LHs can exhibit, especially since these aspects have been thoroughly investigated for Ni-based spinels and perovskites, demonstrating that both Ni atom configuration, as well as the crystal structure, have a significant impact on the OER electrocatalysis.[24,25] For example, in the case of strain-stabilised nickel hydroxide nanoribbons the modification of Ni coordination has a remarkable reduction in the overpotential for OER as well as methanol oxidation reaction (MOR).[24,25] Therefore, the role of the structure and chemical environments in Ni-based LHs emerge as critical to enhance the OER electrochemical activity and stability of these earth-abundant compounds.

In this contribution, we have synthesised and fully characterised Ni-based LHs in the form of the non-expanded β-LH (*brucite*-like structure), and the expanded α-LH and layered double hydroxide (LDH) (*hydrotalcite*-like structure) to assess the role of the crystallographic structure on the OER performance. This is particularly relevant because α-LH phases are often confused with LDH.[26–29] According to structural and theoretical characterisation, the presence of Ni-vacancies in the α-LH phase affects the structural and electronic properties of the LH structure, making it more conductive. In this regard, the electrochemical characterisation confirms a superior catalytic behaviour of α-LH in comparison to the other phases. Specifically, the onset potential is considerably reduced in more than 100 mV for α-LH and the kinetics of the reaction are greatly enhanced due to the inherent high reactivity of the catalytic centres imposed by the presence of Ni-vacancies, which permits the stabilization of Ni^{III} as confirmed by XAS. These findings demonstrate that the crystallographic features play a key role in the electrochemical behaviour of LH phases, pinpointing a new chemical signature for the rational design of more efficient LH-based electrocatalysts.

Results and Discussion

As we have recently reported for Co-based LHs, the role of crystallographic structure can play a crucial role in the OER performance, even in those phases containing Co^{II} cations, exclusively.[23] Thus, considering our last finding and the importance of nickel in the development of OER catalysts, we decided to perform a comprehensive study on the most important Ni-based LHs: *brucite*-like (β-LH), *hydrotalcite*-like (LDH), and turbostratic-like (α-LH). In the case of the non-expanded β-LH phase, cations adopt octahedral environments, $M^{II}(O_h)$, exclusively, and exhibit basal space distances (d_{BS}) lower than 5 Å.[30–32] Without any doubt, the most famous compound of the LH family are layered double hydroxides (LDHs), also known as cationic clays.[16,33] This phase is composed of positively-charged layers containing divalent and trivalent cations located in octahedral environments, $M^{II}(O_h)$ and $M^{III}(O_h)$, respectively. Due to the charge excess, anions and solvent molecules are incorporated in the interlayer space, expanding the d_{BS} to values greater than 7 Å, in accordance with the chemical formula $M^{II}_{1-x}M^{III}_{x}(OH)_2A^{n-}_{x/n}\cdot m(H_2O)$. Thanks to the purely electrostatic anion-sheet interaction, plenty of different LDHs can be obtained by anion exchange reactions, resulting in countless interesting materials for several applications, being nowadays energy storage and conversion the most studied ones.[7,18,33] Additionally, α-LH phases, also known as basic salts, are expanded structures containing anions in the interlayer space.[34,35] The specific crystallographic structure of α-LH phases, as well as the anion-sheet interaction, strongly depends on the nature of the divalent cations, adopting either octahedral (O_h) or tetrahedral (T_d) environments as observed in the case of Co-based LHs. However, the Ni-based α-LH consists of a turbostratic layered hexagonal structure containing $Ni^{II}(O_h)$, exclusively, as represented by the formula $Ni^{Oh}(OH)_{2-x}A^{n-}_{x/n}\cdot m(H_2O)$.[32] Additionally, this layered compound also owns anion exchange properties as in the case of LDHs, even despite the absence of trivalent cations.[36] Figure 1 exemplifies through a schematic representation each Ni-based LHs structure, highlighting their main features. Importantly, since the idea of this work lies in understanding the relationship between the crystallographic structures and electrocatalytic performance, LH phases containing exclusively Ni^{II} as divalent cations are considered. In this regard, an LDH phase containing non-electrocatalytic trivalent cations such as $Al^{III}(O_h)$ is used as a model system.

Ni-based LH phases were obtained through well-established synthetic protocols (see "LH synthesis", in SI), exhibiting sizes lower than 1 μm (Figure S1, SI). Figure 2 compiles the complete chemical and structural characterization of all samples by Powder X-Ray Diffraction (PXRD), Attenuated total reflectance Fourier-transform infrared spectroscopy (ATR-FTIR), X-Ray photoelectron spectroscopy (XPS), UV-Vis spectroscopy and synchrotron X-Ray absorption spectroscopy (XAS).

In the PXRD patterns depicted in Figure 2(A), the presence of reflections at lower 2-*theta* values, indexed as 00*l*, confirms the layered nature of LHs phases. The obtained d_{BS} values are around 4.65, 7.36 and 10.15 Å for β-LH, LDH and α-LH phases, respectively. Furthermore, the reflections labelled as 110, assigned to the intralayer parameter $(a = 2\cdot d_{110})$, provide information about the *in-plane* cationic distances, and exhibit values centred at 1.565, 1.510 and 1.545 Å for β-LH, LDH and α-LH phases, respectively. In the case of the LDH phase, this value is lower than β-LH and α-LH, as expected, due to the incorporation of a smaller cation, Al^{III}, into the layers ($Ni^{II}_{Oh} = 0.690$ Å; $Al^{III}_{Oh} = 0.535$ Å).[37] Table S1 compiles the cell parameters as a function of LH phases, which are in agreement with previous reports.[28,30,31,38,39]

ATR-FTIR also provides relevant structural information about each LH phase, as shown in Figure 2(B). The β-LH phase can be distinguished by the presence of an intense and sharp band at

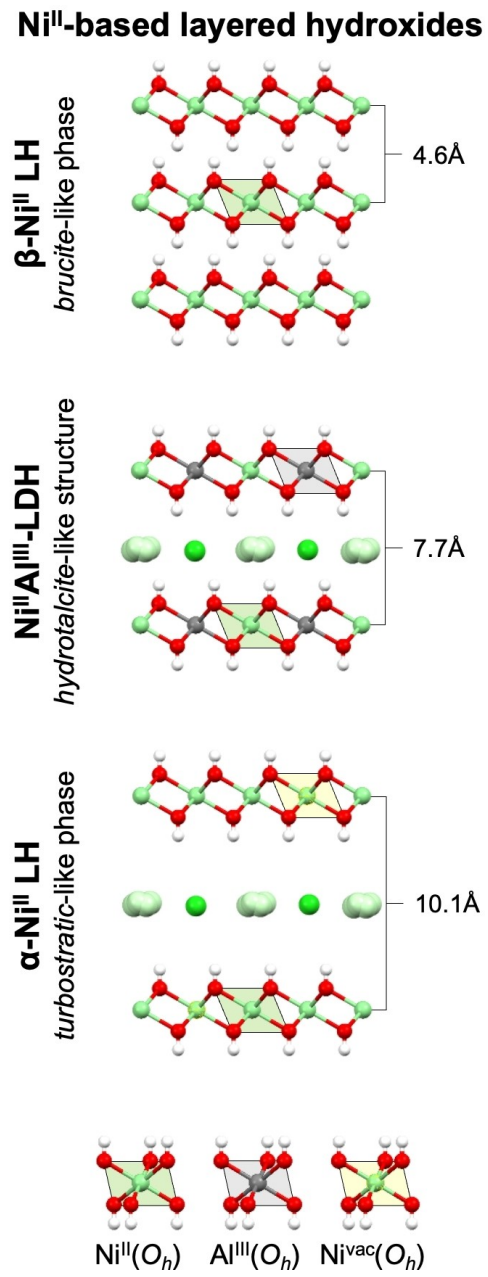

Figure 1. Schematic representation of the different crystallographic structures for Ni-based layered hydroxides studied in this work, highlighting their main differences and reported basal space distances (d_{BS}). Note: Ni^{vac}(O_h) represents a cationic vacancy.

around 3630 cm^{-1} attributed to the O–H stretching mode, characteristic of free-OH groups in *brucite*-like structures.[40] In the case of the expanded structures, the presence of interlayer water molecules can be confirmed by the broad band centred at *ca.* 3400 cm^{-1} (O–H stretching mode) and an extra peak at around 1600 cm^{-1} (H_2O bending mode). The sharper band observed in the α-LH phase is attributed to a higher water confinement degree.[29] Regarding the LDH structure, the bands at 1345 and 800 cm^{-1} confirm the incorporation of carbonate molecules, as expected because of the use of urea as an alkalinisation agent during its synthesis.[41] Finally, the signals below 1000 cm^{-1} are associated with M–O stretching and M–OH bending vibrations. Interestingly, independently of the cation, these vibrations strongly depend on the identity of the LH phase, and are therefore a fingerprint for their easy identification. Table S2 compiles the main characteristic vibration bands for all the LH samples.

XPS was employed to gain further information about the chemical speciation and composition of the samples (Figure 2C). As expected, the presence of Ni^{II} is supported by its main peaks at 856 ± 0.1 eV ($2p^{3/2}$) and 873.5 ± 0.1 eV ($2p^{1/2}$).[42] However, beyond the Ni oxidation state, no appreciable differences are noticeable, suggesting that XPS is not the most appropriate technique for identifying the nature of Ni-based LHs.[43] Further information about the deconvolution spectra and oxidation state can be found in Figure S2 and Table S3, SI.

In contrast, UV-vis diffuse reflectance spectroscopy is a suitable technique in LH characterisation since it can provide information about both metallic coordination environments and oxidation states (Figure 2D), as we demonstrated for Co-LHs structures.[26,44–46] In this regard, Ni-based LHs depict two sets of wide bands positioned around 400 and 700 nm for Ni^{II}(O_h), which are assigned to $^3A_{2g}$ to $^3T_{1g}$(P), $^3T_{1g}$(F), and ^1E_g(D) transitions.[28] Interestingly, the bands ascribable to O_h environments evidence slight differences for each LH phase, indicating changes in the electronic structure. These differences also serve as a convenient fingerprint for identifying the LH samples. Figure S3 and Table S4 compile the positions of these bands for each LH sample.

To further characterise this Ni-based LH family, X-ray absorption spectroscopy (XAS) measurements were conducted in CLÆSS BL22 beamline at ALBA Synchrotron. Figure 2(E) displays the X-ray Absorption Near Edge Structure (XANES) spectra for the Ni–K edge. All the samples contain exclusively Ni^{II}, as confirmed by the position of the absorption edge (in grey). The Extended X-ray Absorption Fine Structure (EXAFS) region was analysed to extract more structural details. Figure 2(F) depicts the Fourier Transform (FT) of the EXAFS oscillations at the Ni K-edge. For all the samples, the two major contributions, located in the 1–3 Å range, represent the average distances (without phase correction) to the first and second coordination shells around the nickel atoms. The pronounced reduction in the second peak amplitude for the LDH sample is related to the presence of Al cations, leading to destructive interferences. Structural parameters such as coordination numbers (*N*), interatomic distances (*R*), and structural disorder (σ^2), were obtained through EXAFS fittings by assuming: (*i*) a single Ni–O distance for O_h cations; (*ii*) a second shell of Ni for β-LH and α-LH samples, and Ni and Al for LDH. The obtained parameters can be found in Table S5, SI. At first glance, for all the samples, Ni^{II} moieties are located in O_h environments, with a Ni–O average coordination number of 5.9 ± 0.2, as expected. The Ni–O distances exhibit values of 2.09 Å for β-LH and LDH, and 2.06 Å for α-LH.[35] The total coordination number obtained for the second shell was 6.1 ± 0.4 and 5.7 ± 0.5 for β-LH and LDH, respectively. However, the α-LH sample exhibits a much lower value of 5.1 ± 0.4. The decrease in the Ni–Ni coordination number can be explained by the existence of Ni-vacancies since

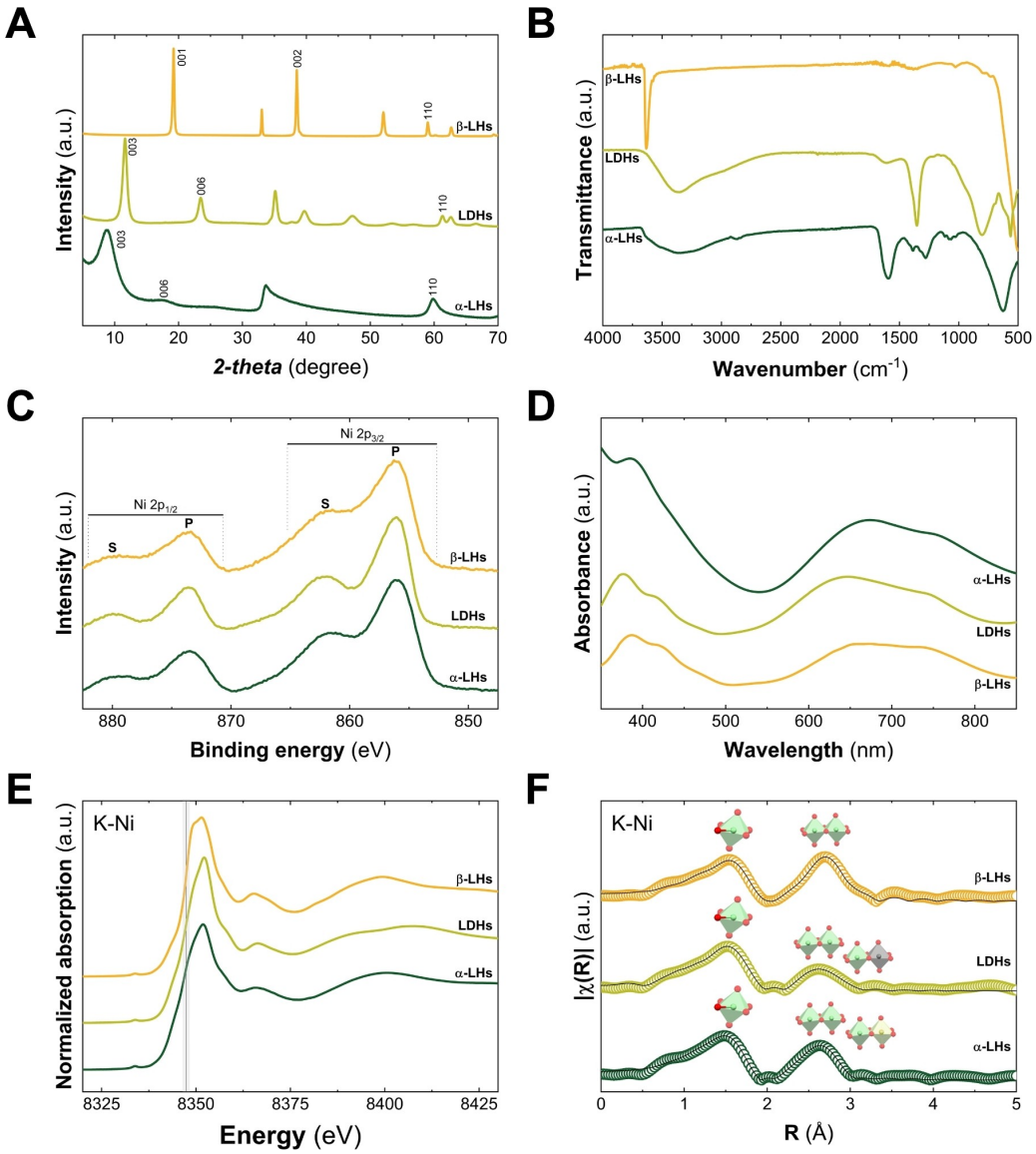

Figure 2. Structural characterisation of Ni-based LHs. A) PXRD patterns underline the layered nature of the structures, as denoted by the *00 l* reflections, while intralayer distance (*a*) is denoted by the 110 reflections. B) ATR-FTIR spectra depict a clear change in the water-related band, highlighting the presence of intralayer water. C) High-resolution XPS for Ni 2p ($2p^{3/2}$ and $2p^{1/2}$) in the range 880–850 eV. D) UV-Vis spectra point out the marked differences in the nickel octahedral environments, $Ni^{II}(O_h)$. E) Normalised XANES spectra at the Ni K-edge. The black line depicts the expected position for nickel atoms exhibiting oxidation state + 2. F) κ^2-weighted Fourier transform of the extracted EXAFS oscillations, for the measured samples -circles- and their corresponding fittings -black line-. The first peaks are attributed at Ni–O distances (green octahedrons). Second peaks consider the Ni–Ni distances (green-green polyhedrons) in the case of β-LHs and α-LHs, and Ni–Ni (green-green polyhedrons) and Ni–Al (green-grey polyhedrons) ones for LDH. The reduction in the intensity for the second peak in the case of α-LHs is attributed to the presence of Ni-vacancies (light green polyhedrons). All the XAS spectra are represented without phase correction.

Ni^{II} cations are exclusively in octahedral sites. This assumption is also in agreement with the higher structural disorder found for this shell/sphere ($\sigma^2_{Ni\text{-}Ni} = 0.011$ Å^2), which suggests a rearrangement of Ni atoms near the vacancies (see Table S5, SI).

Hence, we can confirm the occurrence of Ni-based LHs with non-expanded and expanded structures (*i.e.*, β-LH *vs.* LDH & α-LH, respectively), exclusively composed of Ni^{II} in octahedral environments, where the α-LH phase exhibits cationic vacancies.[47]

To delve into the structural parameters and electronic properties of Ni-based LH phases from a microscopic point of view, *ab-initio* calculations based on density functional theory with Hubbard's correction (DFT + U) were performed. Remarkably, nickel hydroxide in its natural form (*theophrastite*) exhibits a *brucite*-like structure.[48–50] Firstly, we compared our DFT + U simulation for a $\beta - Ni_{DFT+U}$ cell with the structural parameters present in the *theophrastite* phase. After performing atomic relaxations on $\beta - Ni_{DFT+U}$ cell, our results show that the optimised Ni–O and Ni–Ni distances, as well as the most relevant O–Ni-O angles, are in good agreement with those found in the *theophrastite* phase (see Figure S4 and Table S6). For the α-LH phase, there are no reported mineral structures,

and the fundamental structural and electronic aspects are still under discussion.[32] Hence, considering the presence of Ni-vacancies in this structure, as confirmed by EXAFS measurements (Figure 2F),[35,47] we decided to evaluate the role of vacancies in the structural and electronic properties through DFT + U calculations. It is important to remark that our proposition/hypothesis, the $\beta - Ni^{vacancy}_{DFT+U}$ cell, is a simplified simulated structure, serving as a first approximation to the real structure of α-LH phase.

At first glance, the introduction of Ni-vacancies at $\beta - Ni_{DFT+U}$ cell has a great impact on the structural nature of the sheet, producing strong distortions which affect the octahedral environment of Ni^{II} as can be noticed by the changes in interatomic distances and angles (Figure 3A). In the case of the distances, the optimised $\beta - Ni^{vacancy}_{DFT+U}$ cell presents a marked shortening in both Ni–O and Ni–Ni distances in comparison to $\beta - Ni_{DFT+U}$ and, therefore the *theophrastite* phase (Figure S4 and Table S6). Interestingly, these theoretical values are in perfect agreement with the contraction of the *a* parameter observed by PXRD measurements (Figure 2A and Table S1), as well as the shortening in Ni–O and Ni–Ni distances obtained by EXAFS analysis (Figure 2F and Table S5), suggesting that $\beta - Ni^{vacancy}_{DFT+U}$ cell can be considered as a suitable first approximation to study the structural properties of Ni-based α-LH phase. Furthermore, these structural distortions concomitantly modify the O–Ni-O and Ni-O–Ni angles (Figure 3A). Indeed, the optimised structure for the $\beta - Ni^{vacancy}_{DFT+U}$ cell reveals the presence of two kinds of octahedral Ni^{II} cations: a first set of Ni^{II} moieties neighbouring the vacancy (labelled as Niα) and the second set of Ni^{II} sites next-nearest-neighbour to the vacancy (Niβ). While Niα environments, only present in the $\beta - Ni^{vacancy}_{DFT+U}$ cell, are strongly modified by the presence of the vacancy; Niβ environments are equivalent to those ones found in the *theophrastite* phase and both $\beta - Ni_{DFT+U}$ and $\beta - Ni^{vacancy}_{DFT+U}$ cells. Consequently, these differences in the geometrical sites of Ni^{II} cations may explain the observed changes in the optical properties, exemplified by UV-Vis spectroscopy (Figure 2D).

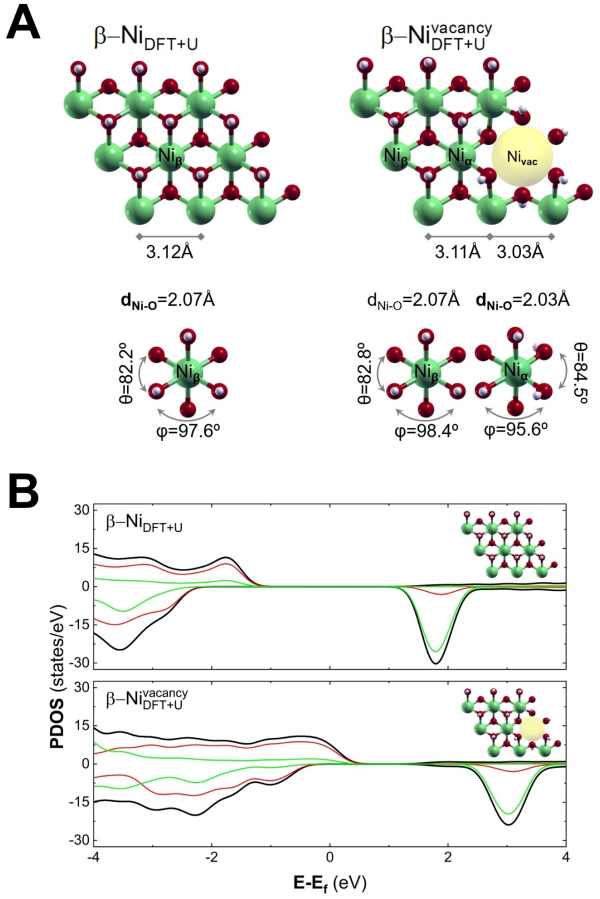

Figure 3. DFT + U simulations for a single layer of *brucitic*-like $Ni(OH)_2$ structure ($\beta - Ni_{DFT+U}$) and the resulting one after the Ni-vacancies generation ($\beta - Ni^{vacancy}_{DFT+U}$). A) Relaxed structures for both supercell highlight that while β-Ni contains only one cationic environment (Ni_β), in the case of β-$Ni^{vacancy}$ presence of two different Ni sites are observed: Ni_α, for the atom around the vacancy, and Ni_β for the other ones. Calculated structural parameters, such as Ni–O and Ni–Ni distances and angles for both supercells are shown. B) Total and Projected Density of States (PDOS) for a layer of β-$Ni(OH)_2$ structure (upper panel) and the resulting one after the generation of Ni-vacancies (lower panel). Atoms are labelled according to Figure 1: H – white, O – red, Ni – green, Ni-vacancy – yellow.

After assessing the structural aspects, we studied the electronic properties. A band gap of approximately 2.2 eV was observed in the case of the $\beta - Ni_{DFT+U}$ cell, indicating an insulator behaviour from the electronic point of view (Figure 3B). An inspection around the Fermi level suggests that the valence band is mainly dominated by the *p* orbitals of oxygen atoms, while conduction bands have a large contribution from the *d* orbitals of Ni cations. As previously mentioned, Ni vacancy generation has a great impact on the structure, which modifies the Ni–O and Ni–Ni distances, as well as the O–Ni-O and Ni-O–Ni angles, resulting in changes in the electronic properties. Indeed, these lattice distortions produce an insulator-metal transition in which both the *p* orbitals of oxygen atoms and the *d* orbitals of Ni atoms shift to the Fermi level. Moreover, it has recently been reported that in α-NiCo LHs the distortion of the octahedral environment, triggered by the shortening of Co–O distances, can promote the population of the Fermi level with *d* states from distorted Co, enhancing their reactivity towards oxidation.[28] This supports the possible modification of the electronic nature of layered materials through the so-called *"cis distortion"*. Additionally, similar electronic behaviour has been observed for NiFe LDHs nanosheets by introducing Ni-vacancies.[51] Although these results strongly suggest that the presence of Ni-vacancies of hydroxylated Ni-based layers would deeply modify the structure, electronic behaviour, and therefore the electrocatalytic performance; strictly speaking, it is important to note that the $\beta - Ni^{vacancy}_{DFT+U}$ cell is a simplified structure for the α-LH phase, and further work is required to provide a comprehensive description of α-Ni LH.

After the structural and electronic description, we performed the electrochemical characterisation of all the samples under alkaline oxygen evolution reaction (OER) conditions, by employing a three-electrode cell (glassy carbon electrode to avoid catalyst-electrode transformation)[52] and using 1 M KOH solution with a purity of 99.98% (Figure 4). Firstly, we proceeded by activating the electroactive material through 30 cyclic voltammetries at a scan rate of 50 mV/s. Remarkably, the cyclic voltammetry curves have a specific shape for each LH

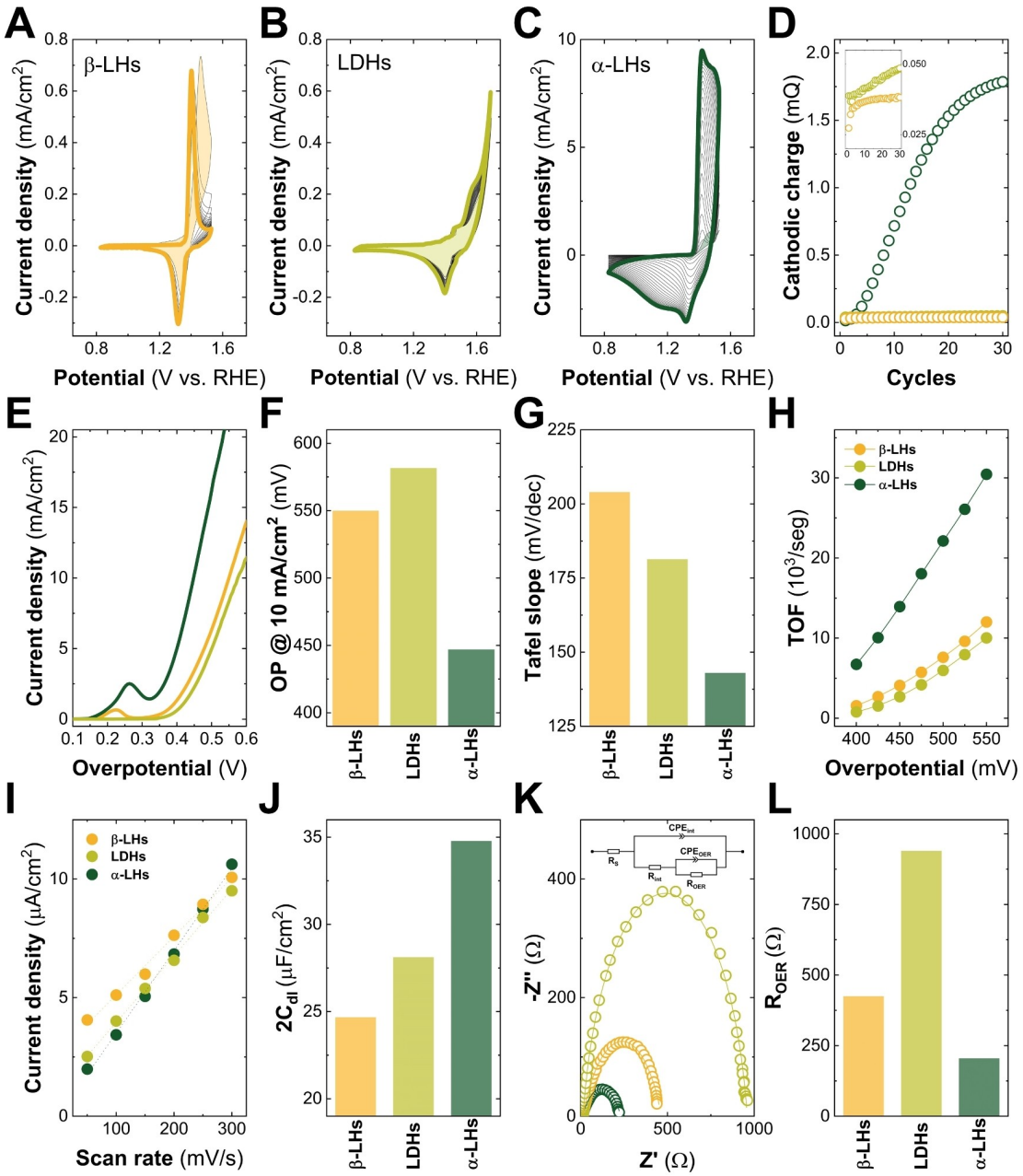

Figure 4. A–C)Activation processes were carried out before the OER experiments and consisted of 30 cyclic voltammetry curves performed in a KOH 1 M aqueous solution at 50 mV/s for each Ni-based LH structure. Note that the orders of magnitude of the *y-axis* are different. The first cycles are depicted as shading curves, while the final ones are presented by thick coloured lines. The shape of the curves as well as their evolution are the first indication of the relationship between structure and electrochemical performance. D) Evolution of the cathodic charge of the different Ni-based LH structures during the activation processes carried out before the OER experiments. Electrochemical characterisation for Ni-based LH family recorded on a glassy carbon electrode collector. E) Linear sweep voltammetry curves measured at 5 mV/s in 1 M KOH aqueous solution. F) Overpotential values required for a current density of 10 mA/cm^2. G) Tafel slopes values calculated from LSV data. H) Turnover frequency values obtained as a function of overpotential. I)Linear slopes representing the ECSA calculated from CVs performed in a non-faradaic region at different scan rates. J) ECSA values of the different structures. K) Nyquist plots of the different samples recorded at an overpotential of 0.4 V. Points correspond to experimental data, and lines are curves fitted with the equivalent circuit. Inset: equivalent circuit used. L) Resistance values of the process associated with the OER. The resistance values were estimated from the equivalent circuit.

sample, suggesting a distinct redox nature for each Ni site, the electroactive species (Figure 4A–C). The activation process was analyzed by extracting the cathodic charge in each cyclic voltammetry curve (Figure 4D). The α-LH sample exhibits the largest activation process (3000 % increment with respect to the first cycle), in comparison to LDH (100 %) and β-LH (35 %). Thus, the superior α-LH activation highlights its inherent chemical nature towards oxidation, which can be mainly related to the presence of Ni-vacancies (and the electronic properties).

Once the samples were activated, the electrochemical water splitting performance was evaluated by measuring linear sweep voltammetry (LSV) at a slow scan rate. The non-*iR* corrected ($R = 2 \pm 1\ \Omega$) overpotential curves measured up to 0.6 V are represented in Figure 4(E). Three key parameters were extracted

from the LSV curves to analyse the OER performance: (*i*) the overpotential (OP) required to get 10 mA/cm^2 (Figure 4F), (*ii*) the Tafel slopes (Figure 4G); and (*iii*) the turnover frequency (TOF) values (Figure 4H), calculated at the overpotential range of 400–525 mV. By comparing all these aforementioned parameters, we can conclude that α-LH arises as the best electroactive material, exhibiting OP values *ca.* 100 mV lower, smaller Tafel slope (*ca.* 32%), and TOF values almost three-fold higher (see Table S7). These results are in good agreement with the ones from the activation process, reinforcing the idea of a higher inherent chemical nature of the α-LH samples towards electrocatalysis.

It is important to remark that some studies have demonstrated that the presence of small transition metal impurities, in particular iron, can lead to inaccurate evaluations of the OER electrochemical performance.[53–56] Therefore, to analyze the potential impact of Fe-based contamination in our experiments, we decided to evaluate the OER performance in purified and Fe-free KOH on glassy carbon electrodes. As depicted in Figure S5 and Table S8, the obtained results (LSV curves, OP and Tafel slope values) confirm the same trend observed in Figure 4: α-LH arises as the best Ni-based OER electrocatalyst of the studied set of LH materials. Specifically, the required OP values to achieve 10 mA/cm^2 do not differ in more than 20 mV between commercial and Fe-free KOH. Hence, the main differences in the short-term OER performance of the three analyzed Ni-based LHs (Figure 4) are mainly associated with their specific crystallographic structures and Ni-vacancies. In any case, further work addressing the long-term Fe-incorporation is being carried out in our laboratory.

To assess the intrinsic reactive and the increment in the number of electroactive centres, the electrochemical surface area (ECSA), corresponding to the double-layer capacitance, was calculated from fitted plots (Figures 4I and J). This value gives an estimation of the number of electroactive centres in the electrocatalyst. In this line, the α-LH phase exhibits an ECSA value around 30–40% larger than the other compounds and thus, it has a higher number of electroactive species able to participate in the OER process, resulting in an enhancement of the electrochemical performance. Additionally, the intrinsic catalytic activities of each material were compared by normalizing the LSV, Tafel slope and TOF results by their respective ECSA values. As a result, the α-LH still exhibits the best figure of merit (Figure S6), demonstrating that this crystallographic structure increases both the amount of electroactive species as well as enhances the specific activity of its Ni^{II} cationic centres towards the OER, as previously suggested by DFT + U calculations.

Then, kinetics aspects were addressed by measuring Electrochemical Impedance Spectroscopy (EIS) and fitting the obtained results to an equivalent circuit (Figure 4K). Due to the possibility of having surface roughness, physical non-uniformity, and non-uniform distribution of the electroactive sites, constant phase elements (CPEs) were introduced in this model to provide a good match with the experimental data. The equivalent circuit is composed of a resistance related to the ionic transport through the solution and the current collectors (R_S) connected in series with a first parallel branch (R_{int} and CPE_{int}) associated with the electrocatalyst-glassy carbon interfacial contact. These elements (R_S, R_{int} and CPE_{int}) are observed in the high-frequency region whereas, in the low-frequency region, OER processes occurring on the LH surface are represented by a second parallel branch (R_{OER} and CPE_{OER}). As can be observed from Figure 4(L), the best values (i.e., the lowest resistances) are once again recorded for the α-LH structure. Indeed, the reduction of R_{OER} is the result of a higher number of active centres and the higher intrinsic conductivity of the electroactive phase, which promotes oxygen formation. Note that for NiAl-LDH, the R_{OER} value is especially high, exceeding that of the β-LH structure. The low formation of the conductive and electroactive NiOOH phase during the OER process may be responsible for this high resistance value in the LDH compound.[57,58] Overall, the increase in the number of electroactive sites in combination with the diminution of the OER resistance results in the improvement of the onset potential, the kinetics of the electrocatalytic reaction, as well as the stability (see Figure S7, Supporting Information).

Considering the differences observed in terms of OER performances, we explored the evolution of the LH phases after the electrocatalytic process. The *ex-situ* characterisation of each LH sample was performed by *in-house* Raman spectroscopy and PXRD immediately after the OER process (less than 1 h), while XAS was carried out after 5 days at ALBA synchrotron. To that end, the samples were deposited by spray coating on carbon paper (C_{paper}) electrodes and electrochemically characterised, obtaining trends similar to those observed on glassy carbon electrodes (see Figure S8, Supporting Information).

Figure 5(A) compares the Raman spectra for LH samples on carbon paper before and after the electrocatalytic process in the 100–1000 cm^{-1} range. Specifically, the main peaks around 400–600 cm^{-1} are assigned to M–O vibrations in all phases. Note that the sensitivity of these two peaks to structural changes during OER has been already studied in some LH phases.[59,60] The β-LH spectra suggest surface oxidation due to the apparition of a broad peak centred at 500 cm^{-1}.[61] LDH spectra do not reveal any observable transformation, as expected considering its poor electrochemical performance. Whilst, in the case of the α-LH sample, the presence of two sharp signals at 476 and 558 cm^{-1} (denoted with asterisks) after OER catalysis evidences the transformation towards the electrocatalytic active NiOOH phase, as previously reported by *in situ* experiments.[62] Furthermore, Figure 5(B) depicts the PXRD patterns of LH samples, where structural modifications are clearly observed. For β-LH, in addition to the presence of unreacted β-$Ni(OH)_2$ signals, the apparition of a new peak at lower *2-theta* values corresponding to an interlayer distance of 7.7 Å highlights the partial transformation towards pure Ni-based LDH phase. Note that, to the best of our knowledge, this is the first structural evidence of a $Ni^{II}Ni^{III}$ LDH structure, indicating the possibility of obtaining this phase through topochemical oxidation.[31,63–65] In contrast, no changes were observed for the LDH sample. Interestingly, in the case of α-LH, the fading of 003 reflection related to this phase suggests a massive transformation toward oxyhydroxide-like phases triggered during the OER process.

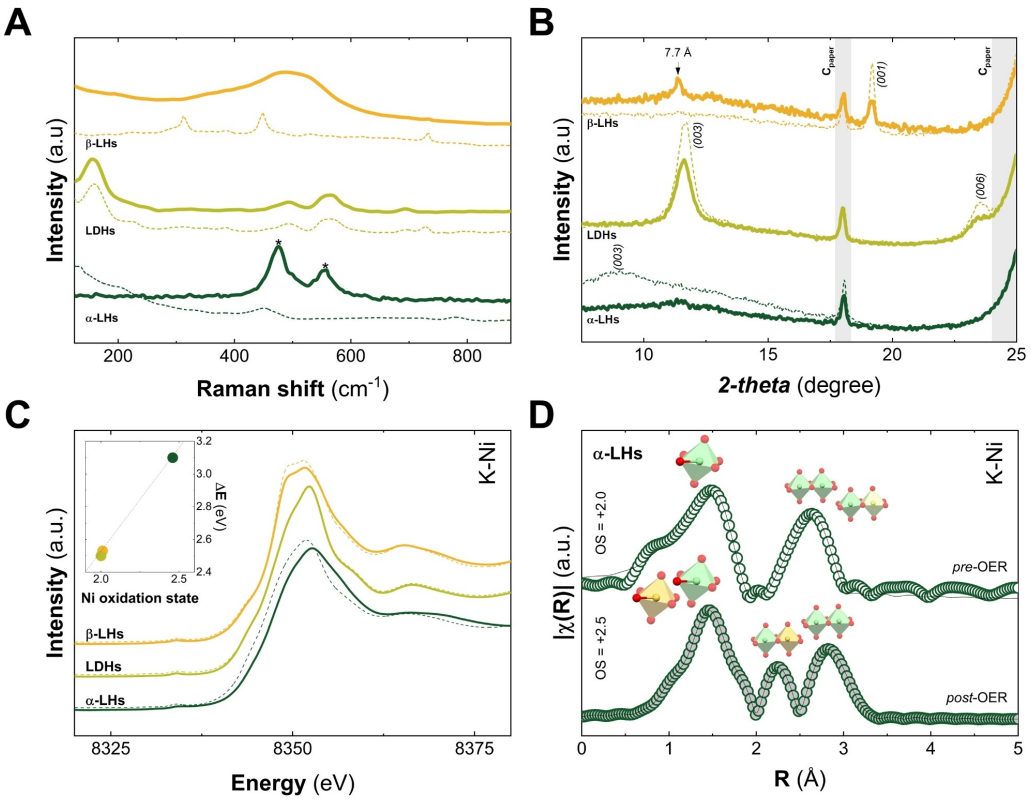

Figure 5. Post-mortem analysis: characterisation before (dashed line) and after (solid line) OER catalysis. A) Raman spectra evidence the surface oxidation of the phases, meanwhile, in the case of α-LH structure, the twin peaks at 476 and 558 cm^{-1} (denoted with asterisks) confirm the transformation into NiOOH. B) PXRD patterns denote non-changes in the bulk structure for β-LH and LDH phases, while in the case of α-LH sample, a massive transformation towards oxyhydroxide-like structure stable under ambient conditions is observable due to the 00*l* signal disappearance. Note: carbon paper substrate (C_{paper}) reflections are denoted in grey. C) Normalised XANES spectra at the Ni K-edge, before (dashed lines, pre-OER) and after (solid lines, post-OER) the OER measurements. Final oxidation states were calculated by Capehart's method after OER measurements and calibration curve (C-inset). D) Pre- and post-OER κ^2-weighted Fourier transform of the extracted EXAFS oscillations for the measured samples – circles – and their corresponding fittings – black line – for α-LH sample. The first peaks are attributed at Ni–O distances: green for $Ni^{II}(O_h)$ and orange for $Ni^{III}(O_h)$. The second and third peaks consider the Ni–Ni distances, where polyhedrons represent: $Ni^{II}(O_h)$ – in green, $Ni^{III}(O_h)$ – in orange, and Ni-vacancies (in light green). In all the cases the XAS spectra are represented without phase correction.

To verify if this transformation into NiOOH after the OER catalysis can be observable in the other samples, we also performed *ex-situ* characterization after 24 h of water splitting reaction. Interestingly, Raman spectra suggest also the formation of NiOOH only in the case of β-LH, but not in the case of LDH, as can be observed by the presence of well-defined and characteristic two main Ni–O vibrations (Figure S9).[62] However, the NiOOH transformation should be exclusively superficial and uncomplete since, even after this long-term catalytic process, the PXRD patterns still exhibit the main characteristic peaks of β-LH and LDH structure, besides the formation of $Ni^{II}Ni^{III}$ LDH phase (Figure S10). Hence, these results confirm the superior intrinsic reactivity in the α-LH phase, which quickly and massively transforms into the stable electroactive oxyhydroxide-like phase during water oxidation.

To further confirm and quantify the changes taking place in the LH samples during the OER catalysis, *ex-situ* XANES spectra were compared before and after the electrocatalytic process (Figure 5C). Almost unnoticeable shifts in the position of the absorption edges are observed for β-LH and LDH samples. However, in the case of α-LH, the shifts become evident, pointing out that this phase is more prone towards oxidation, as observed by Raman and PXRD. A precise quantification of the oxidation state was carried out by employing the integral method described by Capehart *et al.* (Figure 5D).[66] Indeed, while β-LH and LDH do not surpass a final oxidation state higher than 2.1, α-LH sample exhibits a final mean oxidation state of 2.5, which remains remarkably stable under ambient conditions even after weeks. Taking into account the calculated final oxidation states for β-LH and LDH, EXAFS analysis has been carried out on the α-LH sample, exclusively. At first glance, the first peak exhibits a shift towards lower distances, which is consistent with Ni^{III} formation ($Ni^{II}_{Oh} = 0.69$ Å; $Ni^{III}_{Oh} = 0.60$ Å).[37] In the case of the second shell, the original peak splits into two new signals associated with two different Ni–Ni moieties. To quantify this information, a model based on two Ni–O and two Ni–Ni distances is proposed. The results of the fitting are presented in Table S9, Supporting Information. Thus, apart from the previously fitted distances for Ni–O and Ni–Ni of 2.1 and 3.1 Å, the new ones of 1.9 and 2.7 Å are in perfect agreement with the NiOOH formation, which represents approximately

50% of the sample, in concordance with the final oxidation state.[67–69]

Conclusions

Overall, our results confirm that the Ni-based α-LH phase is the most electroactive catalyst among the LH structures containing Ni^{II} centres, exclusively. The structural and theoretical characterisation suggests that the presence of Ni-vacancies affects the structural and electronic properties of the LH phase, making it a more reactive and conductive material, beyond nanostructuration.[24,25,70] In this regard, Ni-vacancies are responsible for this electrochemical enhancement, facilitating its transformation towards highly active and stable oxyhydroxide phases. We envision the α-LH structure as the most appealing host for the incorporation of highly active trivalent cations such as Cr, V, Fe and Co in the search for highly electroactive Ni-based materials for water, methanol and/or ammonia oxidation, with great potential for industrial application.

Experimental Section

Chemicals. Aluminium chloride hexahydrate ($AlCl_3.6H_2O$), ($NiCl_2.6H_2O$), urea, hexamethylenetetramine (HMT), glycidol (Gly), acetylene black, and Nafion (117 solution) were purchased from Sigma-Aldrich. Potassium hydroxide KOH (99.99%) and ethanol absolute (EtOH) were purchased from Panreac. All chemicals were used as received. Milli-Q water was obtained from Millipore Milli-Q equipment.

LH synthesis

Samples were obtained through specific synthetic protocols for each phase. In all the cases, solids were separated for the mother liquors by filtration, washed three times with water, water:ethanol mixture and finally with EtOH. Samples were dried at room temperature and kept in desiccators for further characterization.

Synthesis of β-LH. β-Ni LH sample was synthesised by employing HMT as an alkalinisation reagent following the protocol reported by Liang *et al.*[31] Typically, β-LH precipitation is driven by the hydrolysis of HMT at *ca.* 97 °C for 5 h, under an inert atmosphere, in an aqueous solution containing initial concentrations fixed to: $[NiCl_2 \cdot 6H_2O] = 7.5$ mM and [MHT] = 45 mM.

Synthesis of NiAl LDH. NiAl LDH was synthesised by employing urea as an alkalinisation reagent following the protocol reported by Liu *et al.*[41] Typically, LDH precipitation is driven by the hydrolysis of urea at *ca.* 97 °C for 48 h, under inert an atmosphere, in an aqueous solution containing initial concentrations fixed to: $[NiCl_2 \cdot 6H_2O] =$ 10 mM, $[AlCl_3 \cdot 6H_2O] = 5$ mM, [urea] = 35 mM. In the case of NiAl LDHs the urea concentration was increased to 70 mM.

Synthesis of α-LH. α-Ni LH was synthesised by employing the *Epoxide Route*[38,71] following the protocol reported by Arencibia *et al.*[28,39] Typically, precipitation is driven by the reaction taking place between chloride and Gly at room temperature for 48 h, in an aqueous solution containing initial concentrations fixed to: $[NiCl_2 \cdot 6H_2O] = 10$ mM, [NaCl] = 80 mM, [Gly] = 400 mM.

Chemical and structural characterization

Powder X-ray powder diffraction (PXRD) patterns were obtained employing a PANalytical Empyrean X-ray platform with a capillary platform and copper radiation (Cu Kα = 1.54178 Å). Measurements were carried out by triplicate in the 2-*theta* range 2°–70° by employing a step size of 0.02 °/step with an integration time of 1 s.

Attenuated total reflectance-Fourier transform infrared spectroscopy (ATR-FTIR) spectra were collected in a Bruker alpha II FTIR spectrometer in the 4000–400 cm^{-1} range.

X-ray photoelectron spectroscopy (XPS) measures were recorded in a Thermo Scientific™ K-Alpha X-ray Photoelectron Spectrometer. Al Kα X-ray radiation was employed as an X-ray source. For all the elements more than 100 spectra were recorded employing a step of 0.1 eV with a focused spot higher than 400 μm. XPS data were analysed with Thermo Avantage v5.9912 software.

UV-Vis absorption spectra of the solid samples were recorded in a reflectance mode employing a Jasco V-670 spectrometer.

Individual point Raman spectra were carried out using a Horiba LabRAM HR evolution, employing a blue laser (473 nm) in the 100–1000 cm^{-1} range. For the acquisition of all Raman spectra, a 50x Objective with a 600 mm^{-1} grating was employed. Measurements were performed at least five times at 1.25 mM of laser power, with an acquisition time of 20 seconds.

X-ray absorption spectroscopy

X-ray Absorption Spectroscopy (XAS) measurements were performed at the BL-22 (CLÆSS) beamline from the ALBA synchrotron (Barcelona – Spain). XANES + EXAFS Ni K-edges spectra were measured at room temperature in transmission mode. Absorbents of as-synthesised fresh samples were prepared from powder samples in pellets of 1.3 mm diameter and sealed with Kapton® tape (50 μm in thickness) to prevent the oxidation of the sample. The optimum amount of material for the measurements was calculated by the program Hephaestus which is part of the Demeter package.[72] The pre- and post-OER samples were measured over carbon paper electrodes before and after the OER catalysis. A Si(111) double-crystal monochromator was used to obtain a monochromatic incident beam over the sample. The intensities of the incident and transmitted X-rays were measured using two ionization chambers, respectively. XAS spectra were collected from 8225–9119 eV with a reduced step of 0.3 eV in the XANES region (8325 to 8380 eV) for the Ni K-edge. The incident photon energy was calibrated using the first inflexion point of the Ni K-edge (8333 eV) from reference foils of metallic Ni. For each sample, three spectra were taken with exposure times of 4 min for each one to later be averaged. XANES data treatment was performed by subtracting the pre-edge background followed by normalisation by extrapolating a quadratic polynomial fitted at the post-edge region of the spectrum using ATHENA AUTOBK background removal algorithm.[73] The quantitative analysis of the EXAFS results was performed by modelling and fitting the isolated EXAFS oscillations. The EXAFS oscillations χ(k) were extracted from the experimental data with standard procedures using the Athena program. The k^2 weighted χ(k) data, to enhance the oscillations at higher k, were Fourier transformed. The Fourier transformation was calculated using the Hanning filtering function. EXAFS modelling was carried out using the ARTEMIS software.[72] Theoretical scattering path amplitudes and phase shifts for all paths used in the fits were calculated using the FEFF9 code.[74] The k-range was set from 2.5 to 12.3 $Å^{-1}$. The passive reduction factor S_0^2 values were restrained to 0.83 for Ni, respectively. These values were obtained from the

fitting standard foils of metallic Ni and constraining the coordination numbers to those corresponding to each structure.

Electrochemical characterization

Electrode preparation. For the electrode preparation, a dispersion composed of 2,5 mg of powder material, 1 mL of water and ethanol (1:1) and 7 μL of Nafion (5%) was sonicated in order to obtain a well-dispersed suspension. Then, 5.7 μL was drop-casted in a previously polished (sequentially with 1.0, 0.3 and 0.05 μm alumina powder) 3 mm glassy carbon electrode. Afterwards, the solvent was let evaporated at room temperature. The electrode mass loading achieved was around 0.20 mg cm^{-2}. On the other hand, modified carbon paper electrodes (Toray™ carbon paper with 5% Teflon treated and 0.19 mm thickness, Quintech) were prepared by spray coating the previous dispersion (using an airbrush from Harder Evolution) on carbon papers with a geometrical area of 2×1 cm^2. The electrode mass loading achieved was around 0.50 mg cm^{-2}.

Electrochemical measurements. Electrochemical tests were performed in a three-electrode cell equipped with glassy carbon acting as the working electrode and a platinum wire as the counter electrode. As the reference electrode, a silver-silver chloride (Ag/AgCl (3 M KCl)) was used. All potentials were converted referring to the oxygen evolution reaction overpotential. The measurements were performed on an Autolab PGSTAT 128 N potentiostat/galvanostat. Linear sweep voltammetry (LSV) measurements were carried out at 5 mV s^{-1} in a previously N_2-purged 1 M KOH aqueous solution. Prior to this, 30 cyclic voltammetry measurements were performed at 50 mV s^{-1} to activate the material.

Similar conditions were used to carry out the measurements on modified carbon paper electrodes. However, in this case, another carbon paper with a higher surface area (3×3 cm^2) was used as the counter electrode.

The electrochemical surface area was acquired by measuring the current associated with double-layer capacitance from the scan rate dependence of CVs. The potential range used for the CVs was from −0.25 to −0.05 V versus Ag/AgCl (3 M KCl). The scan rates were 300, 250, 200, 150, 100 and 50 mV s^{-1}. The double-layer capacitance was estimated by plotting the (j_a-j_c) (anodic versus cathodic currents) at −0.15 V versus Ag/AgCl (3 M KCl) against the scan rate. The ECSAs were measured on the working electrodes after performing an activation process consisting of 10 CVs at 50 mV s^{-1} around their redox processes.

The turnover frequency (TOF) values were calculated from the following equation:

$$TOF = jA/4Fn$$

where j is the current density at a given overpotential, A is the surface area of the working electrode, F is the Faraday constant, and n is the total number of moles of the material.

ECSA values were estimated using the following formula:

$$\mathrm{ECSA} = C_{dl} \times A/C_{dl(GCE)}$$

where A is the electrode area, C_{dl} is the double charge capacitance and C_{dl} is the double charge capacitance of the glassy carbon (0.040 mF/cm^2).

Electrochemical impedance spectroscopy (EIS) measurements were carried out using a Gamry 1000E potentiostat/galvanostat controlled by Gamry software by applying an AC amplitude of 10 mV in the frequency range of 10^0–10^5 Hz at an overpotential of 0.40 V. EIS data were analysed and fitted by means of Gamry Echem Analyst v. 7.07 software.

Electrochemical stability tests were done using an Autolab PGSTAT 128N potentiostat/galvanostat.

DFT + U calculations

All the calculations were performed in periodic boundary conditions employing density functional theory (DFT) as implemented in the Quantum Espresso code,[75] which is based on the pseudopotential approximation to represent the ion-electron interactions, and plane waves basis sets to expand the Kohn-Sham orbitals. Ultrasoft-type pseudopotentials were adopted, in combination with the PBE formalism to compute the exchange-correlation term.[76] The magnetic states are described through the Kohn-Sham Hamiltonian in the framework of spin-polarized calculations, plus a Hubbard term. On the basis of our previous reports, the incidence of the Hubbard parameter in the DFT + U calculations on the magnetic coupling and other properties was fixed to 6 eV for Ni atoms.

In all cases, spin-orbit contributions were considered.[77] An energy threshold of 10^{-8} au was used for self-consistency, while for geometry optimization the convergence criteria were 10^{-6} au for the energy and of 10^{-3} au for the forces per atom. To improve the numerical convergence a first-order Methfessel-Paxton spreading was implemented. The van der Waals interactions were considered by including the semiempirical correction DFT-D originally introduced by Grimme[78] and implemented in a plane-wave framework by Barone and co-workers.[79] The simulations were carried out on supercells with specific ordering of the metal polyhedra within the layers. Brillouin zone sampling was performed on these supercells with a Monkhorst-Pack grid, checking for convergence with respect to the number of k-points. A 6×6×1 k-point grid was used in both cases. The atomic structures reported in this work were visualised using XCrysDen.[80]

Supporting Information

Additional references cited within the Supporting Information.[81]

Acknowledgements

This work was supported by the European Research Council (ERC Starting Grant No. 2D-PnictoChem 804110 & ERC PoC 2D4H2 No. 101101079), the Spanish MICINN (PID2019-111742GA–I00, MRR/PDC2022-133997-I00, TED2021-131347B–I00 and Unit of Excellence "Maria de Maeztu" CEX2019-000919-M) and the Generalitat Valenciana (CIDEGENT/2018/001). We thank CELLS-ALBA (Spain) for making all the facilities available for the synchrotron radiation experiment number 2021024897. R.S.-G. thanks to the Spanish Ministry of Universities and the European Union for a 'Margarita Salas' postdoctoral fellowship (Next Generation EU). D.H. thanks CONICET for the financial support and the CNEA-HPC Cluster for the allocation of computational time. A.S.-D thanks the University of Valencia for an 'Atracción del talento' predoctoral

grant. M.M. is a research member from CONICET (Argentina) and thanks to the financial support through the RX-EE-1 project of MinCyT Argentina. The authors thank Ana Alemany-Domenech and Christian Olivares-Martínez for their assistance with the experimental work, and Dr M. D. Jordán Martín for her kind assistance with the XPS measurements. V.O. is an ALN fellow.

Conflict of Interests

The authors declare no conflict of interest.

Data Availability Statement

The data that support the findings of this study are available from the corresponding author upon reasonable request.

Keywords: electrocatalysis · layered hydroxides · water oxidation · DFT

[1] S. Chu, A. Majumdar, *Nature* **2012**, *488*, 294–303.
[2] Z. Yan, J. L. Hitt, J. A. Turner, T. E. Mallouk, *Proc. Natl. Acad. Sci. USA* **2020**, *117*, 12558–12563.
[3] M. F. Lagadec, A. Grimaud, *Nat. Mater.* **2020**, *19*, 1140–1150.
[4] F. Dionigi, Z. Zeng, I. Sinev, T. Merzdorf, S. Deshpande, M. B. Lopez, S. Kunze, I. Zegkinoglou, H. Sarodnik, D. Fan, A. Bergmann, J. Drnec, J. F. de Araujo, M. Gliech, D. Teschner, J. Zhu, W.-X. Li, J. Greeley, B. R. Cuenya, P. Strasser, *Nat. Commun.* **2020**, *11*, 2522.
[5] F. Dionigi, J. Zhu, Z. Zeng, T. Merzdorf, H. Sarodnik, M. Gliech, L. Pan, W.-X. Li, J. Greeley, P. Strasser, *Angew. Chem. Int. Ed.* **2021**, *60*, 14446–14457.
[6] V. Vij, S. Sultan, A. M. Harzandi, A. Meena, J. N. Tiwari, W.-G. Lee, T. Yoon, K. S. Kim, *ACS Catal.* **2017**, *7*, 7196–7225.
[7] D. Zhou, P. Li, X. Lin, A. McKinley, Y. Kuang, W. Liu, W.-F. Lin, X. Sun, X. Duan, *Chem. Soc. Rev.* **2021**, *50*, 8790–8817.
[8] Z. Cai, X. Bu, P. Wang, J. C. Ho, J. Yang, X. Wang, *J. Mater. Chem. A* **2019**, *7*, 5069–5089.
[9] L. Yang, Z. Liu, S. Zhu, L. Feng, W. Xing, *Mater. Today Phys.* **2021**, *16*, 100292.
[10] F. Dionigi, P. Strasser, *Adv. Energy Mater.* **2016**, *6*, 1600621.
[11] M. Gao, W. Sheng, Z. Zhuang, Q. Fang, S. Gu, J. Jiang, Y. Yan, *J. Am. Chem. Soc.* **2014**, *136*, 7077–7084.
[12] O. Diaz-Morales, I. Ledezma-Yanez, M. T. M. Koper, F. Calle-Vallejo, *ACS Catal.* **2015**, *5*, 5380–5387.
[13] J. Deng, M. R. Nellist, M. B. Stevens, C. Dette, Y. Wang, S. W. Boettcher, *Nano Lett.* **2017**, *17*, 6922–6926.
[14] Y. Chen, K. Rui, J. Zhu, S. X. Dou, W. Sun, *Chemistry A European J.* **2019**, *25*, 703–713.
[15] F. Li, X. Duan, in *Layered Double Hydroxides* (Eds.: X. Duan, D. G. Evans), Springer, Berlin, Heidelberg, **2006**, pp. 193–223.
[16] S. He, Z. An, M. Wei, D. G. Evans, X. Duan, *Chem. Commun.* **2013**, *49*, 5912–5920.
[17] G. Fan, F. Li, D. G. Evans, X. Duan, *Chem. Soc. Rev.* **2014**, *43*, 7040–7066.
[18] J. Yu, Q. Wang, D. O'Hare, L. Sun, *Chem. Soc. Rev.* **2017**, *46*, 5950–5974.
[19] C. Luan, G. Liu, Y. Liu, L. Yu, Y. Wang, Y. Xiao, H. Qiao, X. Dai, X. Zhang, *ACS Nano* **2018**, *12*, 3875–3885.
[20] J. A. Carrasco, R. Sanchis-Gual, A. S.-D. Silva, G. Abellán, E. Coronado, *Chem. Mater.* **2019**, *31*, 6798–6807.
[21] S. Sun, C. Lv, W. Hong, X. Zhou, F. Wu, G. Chen, *ACS Appl. Energ. Mater.* **2019**, *2*, 312–319.
[22] Y. Dong, S. Komarneni, F. Zhang, N. Wang, M. Terrones, W. Hu, W. Huang, *Appl. Catal. B* **2020**, *263*, 118343.
[23] R. Sanchis-Gual, D. Hunt, C. Jaramillo-Hernández, A. Seijas-Da Silva, M. Mizrahi, C. Marini, V. Oestreicher, G. Abellán, *ACS Catal.* **2023**, *13*, 10351–10363.
[24] X. P. Wang, H. J. Wu, S. B. Xi, W. S. V. Lee, J. Zhang, Z. H. Wu, J. O. Wang, T. D. Hu, L. M. Liu, Y. Han, S. W. Chee, S. C. Ning, U. Mirsaidov, Z. B. Wang, Y. W. Zhang, A. Borgna, J. Wang, Y. H. Du, Z. G. Yu, S. J. Pennycook, J. M. Xue, *Energy Environ. Sci.* **2020**, *13*, 229–237.
[25] X. Wang, S. Xi, W. S. V. Lee, P. Huang, P. Cui, L. Zhao, W. Hao, X. Zhao, Z. Wang, H. Wu, H. Wang, C. Diao, A. Borgna, Y. Du, Z. G. Yu, S. Pennycook, J. Xue, *Nat. Commun.* **2020**, *11*, 4647.
[26] R. Ma, Z. Liu, K. Takada, K. Fukuda, Y. Ebina, Y. Bando, T. Sasaki, *Inorg. Chem.* **2006**, *45*, 3964–3969.
[27] Y. Du, D. O'Hare, *Inorg. Chem.* **2008**, *47*, 3234–3242.
[28] D. Hunt, V. Oestreicher, M. Mizrahi, F. G. Requejo, M. Jobbágy, *Chem. Eur. J.* **2020**, *26*, 17081–17090.
[29] V. Oestreicher, G. Abellán, E. Coronado, *Phys. status solidi Rapid Res. Lett.* **2020**, *14*, 2000380.
[30] G. J. de A. A. Soler-Illia, M. Jobbágy, A. E. Regazzoni, M. A. Blesa, *Chem. Mater.* **1999**, *11*, 3140–3146.
[31] J. Liang, R. Ma, N. Iyi, Y. Ebina, K. Takada, T. Sasaki, *Chem. Mater.* **2010**, *22*, 371–378.
[32] D. S. Hall, D. J. Lockwood, C. Bock, B. R. MacDougall, *Proc. Roy. Soc. A* **2015**, *471*, 20140792.
[33] Q. Wang, D. O'Hare, *Chem. Rev.* **2012**, *112*, 4124–4155.
[34] M. Taibi, S. Ammar, N. Jouini, F. Fiévet, P. Molinié, M. Drillon, *J. Mater. Chem.* **2002**, *12*, 3238–3244.
[35] M. Taibi, N. Jouini, P. Rabu, S. Ammar, F. Fiévet, *J. Mater. Chem. C* **2014**, *2*, 4449–4460.
[36] P. V. Kamath, G. H. Annal Therese, J. Gopalakrishnan, *J. Solid State Chem.* **1997**, *128*, 38–41.
[37] R. D. Shannon, *Acta Crystallogr. Sect. A* **1976**, *32*, 751–767.
[38] V. Oestreicher, I. Fábregas, M. Jobbágy, *J. Phys. Chem. C* **2014**, *118*, 30274–30281.
[39] N. Arencibia, V. Oestreicher, F. A. Viva, M. Jobbágy, *RSC Adv.* **2017**, *7*, 5595–5600.
[40] Z. Liu, R. Ma, M. Osada, K. Takada, T. Sasaki, *J. Am. Chem. Soc.* **2005**, *127*, 13869–13874.
[41] Z. Liu, R. Ma, M. Osada, N. Iyi, Y. Ebina, K. Takada, T. Sasaki, *J. Am. Chem. Soc.* **2006**, *128*, 4872–4880.
[42] M. C. Biesinger, B. P. Payne, A. P. Grosvenor, L. W. M. Lau, A. R. Gerson, R. St. C. Smart, *Appl. Surf. Sci.* **2011**, *257*, 2717–2730.
[43] V. Oestreicher, C. Dolle, D. Hunt, M. Fickert, G. Abellán, *Nano Mater. Sci.* **2022**, *4*, 36–43.
[44] J. R. Neilson, B. Schwenzer, R. Seshadri, D. E. Morse, *Inorg. Chem.* **2009**, *48*, 11017–11023.
[45] V. Oestreicher, D. Hunt, R. Torres-Cavanillas, G. Abellán, D. A. Scherlis, M. Jobbágy, *Inorg. Chem.* **2019**, *58*, 9414–9424.
[46] V. Oestreicher, D. Hunt, C. Dolle, P. Borovik, M. Jobbágy, G. Abellán, E. Coronado, *Chem. Eur. J.* **2021**, *27*, 921–927.
[47] Q. He, Y. Wan, H. Jiang, Z. Pan, C. Wu, M. Wang, X. Wu, B. Ye, P. M. Ajayan, L. Song, *ACS Energy Lett.* **2018**, *3*, 1373–1380.
[48] R. W. Cairns, E. Ott, *J. Am. Chem. Soc.* **1933**, *55*, 527–533.
[49] J. Zemann, *Acta Crystallogr.* **1965**, *18*, 139–139.
[50] T. N. Ramesh, P. V. Kamath, C. Shivakumara, *Acta Crystallogr. Sect. B* **2006**, *62*, 530–536.
[51] Y. Wang, M. Qiao, Y. Li, S. Wang, *Small* **2018**, *14*, 1800136.
[52] A. S.-D. Silva, V. Oestreicher, E. Coronado, G. Abellán, *Dalton Trans.* **2022**, *51*, 4675–4684.
[53] A. C. Garcia, T. Touzalin, C. Nieuwland, N. Perini, M. T. M. Koper, *Angew. Chem. Int. Ed.* **2019**, *58*, 12999–13003.
[54] R. A. Márquez, K. Kawashima, Y. J. Son, G. Castelino, N. Miller, L. A. Smith, C. E. Chukwuneke, C. B. Mullins, *ACS Energy Lett.* **2023**, *8*, 1141–1146.
[55] L. Trotochaud, S. L. Young, J. K. Ranney, S. W. Boettcher, *J. Am. Chem. Soc.* **2014**, *136*, 6744–6753.
[56] S. Anantharaj, S. Kundu, S. Noda, *Nano Energy* **2021**, *80*, 105514.
[57] Z. Lu, W. Xu, W. Zhu, Q. Yang, X. Lei, J. Liu, Y. Li, X. Sun, X. Duan, *Chem. Commun.* **2014**, *50*, 6479–6482.
[58] J. Zhang, J. Liu, L. Xi, Y. Yu, N. Chen, S. Sun, W. Wang, K. M. Lange, B. Zhang, *J. Am. Chem. Soc.* **2018**, *140*, 3876–3879.
[59] M. Steimecke, G. Seiffarth, C. Schneemann, F. Oehler, S. Förster, M. Bron, *ACS Catal.* **2020**, *10*, 3595–3603.
[60] H. Radinger, P. Connor, S. Tengeler, R. W. Stark, W. Jaegermann, B. Kaiser, *Chem. Mater.* **2021**, *33*, 8259–8266.
[61] S. Klaus, Y. Cai, M. W. Louie, L. Trotochaud, A. T. Bell, *J. Phys. Chem. C* **2015**, *119*, 7243–7254.
[62] J. D. Michael, E. L. Demeter, S. M. Illes, Q. Fan, J. R. Boes, J. R. Kitchin, *J. Phys. Chem. C* **2015**, *119*, 11475–11481.

[63] R. Ma, Z. Liu, K. Takada, N. Iyi, Y. Bando, T. Sasaki, *J. Am. Chem. Soc.* **2007**, *129*, 5257–5263.
[64] R. Ma, K. Takada, K. Fukuda, N. Iyi, Y. Bando, T. Sasaki, *Angew. Chem. Int. Ed.* **2008**, *47*, 86–89.
[65] Y. He, X. Liu, G. Chen, J. Pan, A. Yan, A. Li, X. Lu, D. Tang, N. Zhang, T. Qiu, R. Ma, T. Sasaki, *Chem. Mater.* **2020**, *32*, 4232–4240.
[66] T. W. Capehart, J. F. Herbst, R. K. Mishra, F. E. Pinkerton, *Phys. Rev. B* **1995**, *52*, 7907–7914.
[67] R. Barnard, C. F. Randell, F. L. Tye, *J. Appl. Electrochem.* **1980**, *10*, 109–125.
[68] J. McBreen, W. E. O'Grady, G. Tourillon, E. Dartyge, A. Fontaine, K. I. Pandya, *J. Phys. Chem.* **1989**, *93*, 6308–6311.
[69] Y.-F. Li, J.-L. Li, Z.-P. Liu, *J. Phys. Chem. C* **2021**, *125*, 27033–27045.
[70] N. Tarutani, Y. Tokudome, M. Jobbágy, G. J. A. A. Soler-Illia, M. Takahashi, *J. Mater. Chem. A* **2019**, *7*, 25290–25296.
[71] V. Oestreicher, M. Jobbágy, *Langmuir* **2013**, *29*, 12104–12109.
[72] B. Ravel, M. Newville, *J. Synchrotron Radiat.* **2005**, *12*, 537–541.
[73] M. Newville, IUCr, IFEFFIT, http://scripts.iucr.org/cgi-bin/paper?S0909049500016964, (accessed 23 May 2022).
[74] J. J. Rehr, J. J. Kas, F. D. Vila, M. P. Prange, K. Jorissen, *Phys. Chem. Chem. Phys.* **2010**, *12*, 5503–5513.
[75] P. Giannozzi, S. Baroni, N. Bonini, M. Calandra, R. Car, C. Cavazzoni, D. Ceresoli, G. L. Chiarotti, M. Cococcioni, I. Dabo, A. D. Corso, S. de Gironcoli, S. Fabris, G. Fratesi, R. Gebauer, U. Gerstmann, C. Gougoussis, A. Kokalj, M. Lazzeri, L. Martin-Samos, N. Marzari, F. Mauri, R. Mazzarello, S. Paolini, A. Pasquarello, L. Paulatto, C. Sbraccia, S. Scandolo, G. Sclauzero, A. P. Seitsonen, A. Smogunov, P. Umari, R. M. Wentzcovitch, *J. Phys. Condens. Matter* **2009**, *21*, 395502.
[76] J. P. Perdew, K. Burke, M. Ernzerhof, *Phys. Rev. Lett.* **1996**, *77*, 3865–3868.
[77] A. D. Corso, A. M. Conte, *Phys. Rev. B* **2005**, *71*, 115106.
[78] S. Grimme, *J. Comput. Chem.* **2006**, *27*, 1787–1799.
[79] V. Barone, M. Casarin, D. Forrer, M. Pavone, M. Sambi, A. Vittadini, *J. Comput. Chem.* **2009**, *30*, 934–939.
[80] A. Kokalj, *J. Mol. Graphics Modell.* **1999**, *17*, 176–179.
[81] J. D. Michael, E. L. Demeter, S. M. Illes, Q. Fan, J. R. Boes, J. R. Kitchin, *J. Phys. Chem. C* **2015**, *119*, 11475–11481.

Manuscript received: September 26, 2023
Accepted manuscript online: November 15, 2023
Version of record online: November 29, 2023